for the graphene monolayer (as in Figs. 2 and 3). For the bilayer, we increased the conductivity to match the experimental wavelength ratio, $\lambda_{p,1} = 1.4\lambda_p$ (Fig. 4H). We measured $\alpha_1 = 50°$ and $\alpha_2 = 30°$, yielding $\sin(\alpha_1)/\sin(\alpha_2) = 1.53$, qualitatively following Snell's law (Eq. 1). The quantitative discrepancy found in both experiment and theory [i.e., $\sin(\alpha_1)/\sin(\alpha_2) > \lambda_{p,1}/\lambda_{p,2}$] is attributed to the strong GP damping. In strongly absorbing media, Snell's law deviates from its simple form (Eq. 1), as fronts of constant amplitude and phase may exhibit different diffraction angles (31), which is not considered in our analysis. Although further studies are required for a better quantitative understanding, our results demonstrate that GP propagation can be controlled by refraction. In the future, local gating of graphene could open exciting avenues for electrically tunable refractive elements, such as for steering of GPs.

Launching and control of propagating GPs by resonant metal antennas and spatial conductivity patterns could lead to various applications, including GP focusing into gated graphene waveguides, resonators, modulators, or plasmon interferometers for communication and sensing. Through the use of improved doping strategies and carrier mobility in graphene, we expect GPs to propagate over distances of many wavelengths at mid-infrared, near-infrared, and telecommunication wavelengths. Resonant antenna devices might also be used for converting the GPs into far-field radiation, which would enable a purely optical readout of graphene plasmonic circuits or wireless on-chip communication between them.

REFERENCES AND NOTES

1. W. L. Barnes, A. Dereux, T. W. Ebbesen, *Nature* **424**, 824–830 (2003).
2. S. A. Maier, *Plasmonics: Fundamentals and Applications* (Springer-Verlag, New York, 2007).
3. P. Mühlschlegel, H. J. Eisler, O. J. F. Martin, B. Hecht, D. W. Pohl, *Science* **308**, 1607–1609 (2005).
4. S. I. Bozhevolnyi, V. S. Volkov, E. Devaux, J.-Y. Laluet, T. W. Ebbesen, *Nature* **440**, 508–511 (2006).
5. F. López-Tejeira et al., *Nat. Phys.* **3**, 324–328 (2007).
6. J. Lin et al., *Science* **340**, 331–334 (2013).
7. F. J. Rodríguez-Fortuño et al., *Science* **340**, 328–330 (2013).
8. A. Boltasseva, H. A. Atwater, *Science* **331**, 290–291 (2011).
9. K. W. K. Shung, *Phys. Rev. B* **34**, 979–993 (1986).
10. O. Vafek, *Phys. Rev. Lett.* **97**, 266406 (2006).
11. G. W. Hanson, *J. Appl. Phys.* **103**, 064302 (2008).
12. M. Jablan, H. Buljan, M. Soljačić, *Phys. Rev. B* **80**, 245435 (2009).
13. B. Wunsch, T. Stauber, F. Sols, F. Guinea, *New J. Phys.* **8**, 318 (2006).
14. M. Polini et al., *Phys. Rev. B* **77**, 081411 (2008).
15. A. Vakil, N. Engheta, *Science* **332**, 1291–1294 (2011).
16. F. Zang et al., *ACS Nano* **6**, 10222–10228 (2012).
17. Y. Yao et al., *Nano Lett.* **13**, 1257–1264 (2013).
18. H. Yan et al., *Nat. Photonics* **7**, 394–399 (2013).
19. L. Ju et al., *Nat. Nanotechnol.* **6**, 630–634 (2011).
20. A. N. Grigorenko, M. Polini, K. S. Novoselov, *Nat. Photonics* **6**, 749–758 (2012).
21. F. J. García de Abajo, *Science* **339**, 917–918 (2013).
22. A. Y. Nikitin, F. Guinea, F. J. Garcia-Vidal, L. Martin-Moreno, *Phys. Rev. B* **84**, 195446 (2011).
23. F. H. L. Koppens, D. E. Chang, F. J. García de Abajo, *Nano Lett.* **11**, 3370–3377 (2011).
24. J. Chen et al., *Nature* **487**, 77–81 (2012).
25. Z. Fei et al., *Nature* **487**, 82–85 (2012).
26. See supplementary materials on *Science* Online.
27. Y. Liu et al., *Nano Lett.* **12**, 4853–4858 (2012).
28. M. Schnell et al., *Nat. Photonics* **3**, 287–291 (2009).
29. H. Yan et al., *Nat. Nanotechnol.* **7**, 330–334 (2012).
30. Y.-M. Lin et al., *Nano Lett.* **8**, 2119 (2008).
31. M. Born, E. Wolf, *Principles of Optics* (Pergamon, New York, 1959).

LOW-DENSITY MATERIALS

Ultralight, Ultrastiff Mechanical Metamaterials

Xiaoyu Zheng,[1]* Howon Lee,[2] Todd H. Weisgraber,[1] Maxim Shusteff,[1] Joshua DeOtte,[1] Eric B. Duoss,[1] Joshua D. Kuntz,[1] Monika M. Biener,[1] Qi Ge,[2] Julie A. Jackson,[1] Sergei O. Kucheyev,[1] Nicholas X. Fang,[2]* Christopher M. Spadaccini[1]*

The mechanical properties of ordinary materials degrade substantially with reduced density because their structural elements bend under applied load. We report a class of microarchitected materials that maintain a nearly constant stiffness per unit mass density, even at ultralow density. This performance derives from a network of nearly isotropic microscale unit cells with high structural connectivity and nanoscale features, whose structural members are designed to carry loads in tension or compression. Production of these microlattices, with polymers, metals, or ceramics as constituent materials, is made possible by projection microstereolithography (an additive micromanufacturing technique) combined with nanoscale coating and postprocessing. We found that these materials exhibit ultrastiff properties across more than three orders of magnitude in density, regardless of the constituent material.

Nature has found a way to achieve mechanically efficient materials by evolving cellular structures. Natural cellular materials, including honeycomb (1) (wood, cork) and foamlike structures, such as trabecular bone (2), plant parenchyma (3), and sponge (4), combine low weight with superior mechanical properties. For example, lightweight balsa has a stiffness-to-weight ratio comparable to that of steel along the axial loading direction (5). Inspired by these naturally occurring cellular structures, human-made lightweight cellular materials fabricated from a wide array of solid constituents are desirable for a broad range of applications including structural components (6, 7), energy absorption (8, 9), heat exchange (10, 11), catalyst supports (12), filtration (13, 14), and biomaterials (15, 16).

However, the degradation in mechanical properties can be drastic as density decreases (17, 18). A number of examples among recently reported low-density materials include graphene elastomers (19), metallic microlattices (20), carbon nanotube foams (21), and silica aerogels (22, 23). For instance, the Young's modulus of low-density silica aerogels (22, 23) decreases to 10 kPa (0.00001% of bulk) at a density of less than 10 mg/cm^3 (<0.5% of bulk).

This loss of mechanical performance is because most natural and engineered cellular solids with random porosity, particularly at relative densities less than 0.1%, exhibit a quadratic or stronger scaling relationship between Young's modulus and density as well as between strength and density. Namely, $E/E_s \propto (\rho/\rho_s)^n$ and $\sigma_y/\sigma_{ys} \propto (\rho/\rho_s)^n$, where E is Young's modulus, ρ is density, σ_y is yield strength, and s denotes the respective bulk value of the solid constituent material property. The power n of the scaling relationship between relative material density and the relative mechanical property depends on the material's microarchitecture. Conventional cellular foam materials with stochastic porosity

[1]Lawrence Livermore National Laboratory, Livermore, CA 94550, USA. [2]Department of Mechanical Engineering, Massachusetts Institute of Technology, Cambridge, MA 02139, USA.

*Corresponding author. E-mail: zheng3@llnl.gov (X.Z.); spadaccini2@llnl.gov (C.M.S.); nicfang@mit.edu (N.X.F.)

are known to deform predominantly through bending of their cell walls and struts (24). This type of deformation results in relative stiffness scaling with $n = 2$ or 3. A number of approaches in recent years have aimed to reduce this coupling between mechanical properties and mass density (5, 17, 18, 20, 25–31). Among these, few fabrication processes are capable of building arbitrary three-dimensional microarchitectures with controlled micro- and nanostructure across a wide range of mass density and material constituents. The desired material properties are thus limited to a narrow density range and specific loading directions.

Improved mechanical properties can arise from a material that contains micro- and nanoscale building blocks arranged in an ordered hierarchy. Among these new designs are metallic microlattices with high recoverability when compressed (20, 26), TiN nanotrusses (32, 33), and ceramic composite trusses (34) that show enhanced fracture toughness of coating materials when the thickness of coating materials is reduced to the nanoscale.

We report a group of ultralight mechanical metamaterials that maintain a nearly linear scaling between stiffness and density spanning three orders of magnitude in density, over a variety of constituent materials. We use the term "mechanical metamaterials" to refer to materials with certain mechanical properties defined by their geometry rather than their composition. The materials described here are highly ordered, nearly isotropic, and have high structural connectivity within stretch-dominated, face-centered cubic (fcc) architectures. The ultralow-density regime is accessed by fabricating microlattices with critical features ranging from ~20 μm down to ~40 nm. The densities of samples produced in this work ranged from 0.87 kg/m³ to 468 kg/m³, corresponding to 0.025% to 20% relative density.

A stretch-dominated unit cell structure, consisting of b struts and j frictionless joints and satisfying Maxwell's criterion, $M = b - 3j + 6 > 0$, is substantially more mechanically efficient—with a higher stiffness-to-weight ratio (defined as E/ρ)—than its bend-dominated counterpart. This is attributed to its struts carrying load under compression or tension rather than bending (17). A fundamental lattice building block of this type is the octet-truss unit cell (Fig. 1A), whose geometric configuration was proposed by Deshpande et al. (35). The cell has a regular octahedron as its core, surrounded by eight regular tetrahedra distributed on its faces (fig. S1). All the strut elements have identical aspect ratios, with 12 solid rods or hollow tubes connected at each node. The cubic symmetry of the cell's fcc structure generates a material with nearly isotropic behavior (36). The relative density of such octet-truss unit cells can be approximated by $\rho = 26.64(d/L)^2$ (35), where L and d are the length and diameter of each beam element. On the macroscale, under uniaxial compressive loading, the relative compressive stiffness and yield strength of these structures theoretically show linear scaling relationships: $E/E_s \propto (\rho/\rho_s)$ and

$\sigma/\sigma_s \propto (\rho/\rho_s)$ (35). A cubic lattice is readily constructed by periodic packing of the unit cell along its three principal directions (Fig. 1, B and C) (37, 38). Alternate orientations of the bulk lattice relative to the unit cell's principal axes can likewise be constructed (fig. S2), with the fundamental tessellation of space by the unit cell remaining the same.

To study how the loading direction and lattice orientation of an octet-truss lattice affects its E-ρ scaling relationship, we analyzed, fabricated, and tested them in a variety of orientations (39) (figs. S1 to S5). In addition to these stretch-dominated lattices, as a point of comparison, a bend-dominated tetrakaidecahedron unit cell (40, 41) of the same size scale was generated and the corresponding cubic-symmetric foams (known as Kelvin foams) were fabricated with a variety of densities (Fig. 1, D to F).

The fabrication of these microlattices is enabled by projection microstereolithography, a layer-by-layer additive micromanufacturing process capable of fabricating arbitrary three-dimensional microscale structures (42, 43). In contrast to other three-dimensional (3D) rapid prototyping methods such as 3D printing and ultraviolet (UV) projection waveguide systems (44), this type of fabrication technology is ideal for 3D lattices with high structural complexity and with feature sizes ranging from tens of micrometers to centimeters. By combining projection microstereolithography with nanoscale coating methods, 3D lattices with ultralow relative densities below 0.1% can be created. The process begins with a photosensitive polymer resin bath; we use either 1,6-hexanediol diacrylate (HDDA)

or poly(ethylene glycol) diacrylate (PEGDA). Shown schematically in Fig. 2A, the apparatus uses a spatial light modulator—in this case a liquid-crystal-on-silicon chip—as a dynamically reconfigurable digital photomask. A three-dimensional CAD model is first sliced into a series of closely spaced horizontal planes. These two-dimensional image slices are sequentially transmitted to the reflective liquid-crystal-on-silicon chip, which is illuminated with UV light from a light-emitting diode array. Each image is projected through a reduction lens onto the surface of the photosensitive resin. The exposed liquid cures, forming a layer in the shape of the two-dimensional image, and the substrate on which it rests is lowered, reflowing a thin film of liquid over the cured layer. The image projection is then repeated, with the next image slice forming the subsequent layer. Our polymer microlattices were fabricated in tens of minutes and have features spanning size scales from 10 to 500 μm. For mechanical testing purposes, all materials described here were fabricated as blocks of various sizes consisting of multiple unit cells (table S1). Scanning electron microscopy (SEM) images of the as-built polymer lattice and unit cell are shown in Fig. 2, B and F.

Although projection microstereolithography requires a photopolymer, other constituent materials such as metals and ceramics can be incorporated with additional processing. Using the base polymer lattice as a template, we are able to convert the structures to metallic and ceramic microlattices. Metallic lattices were generated via electroless nickel plating on the as-formed HDDA. The thickness of the metal coating is
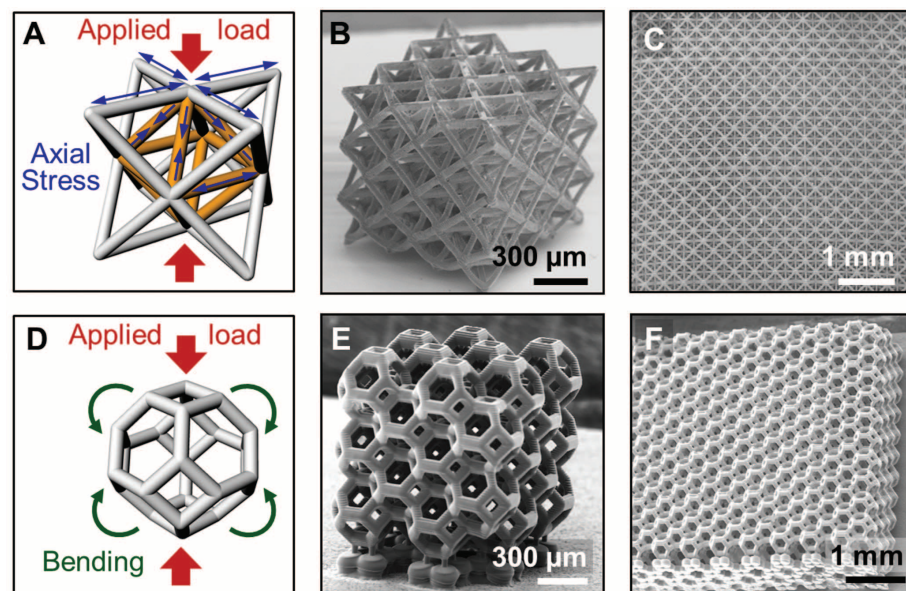

Fig. 1. Architecture of stretch-dominated and bend-dominated unit cells and lattices. (**A**) Mechanical response to compressive loading of a stretch-dominated octet-truss unit cell. (**B**) Octet-truss unit cells packed into a cubic microlattice. (**C**) SEM image of a stretch-dominated lattice material composed of a network of octet-truss unit cells. (**D**) Mechanical response to compressive loading of a bend-dominated tetrakaidecahedron unit cell. (**E**) Tetrakaidecahedron unit cell packed into a cubic bend-dominated lattice (Kelvin foam). (**F**) SEM image of a bend-dominated lattice composed of a network of tetrakaidecahedron unit cells.

controlled by the plating time, yielding metal films from 100 nm to 2 μm. The polymer template is subsequently removed by thermal decomposition, leaving behind the hollow-tube nickel-phosphorus (Ni-P) stretch-dominated microlattice shown in Fig. 2, C and G.

A similar templating approach is used to generate hollow-tube aluminum oxide (amorphous Al_2O_3, alumina) microlattices; however, the coating is produced by atomic layer deposition (ALD), a gas-phase process, rather than liquid-phase processing. The resulting hollow-tube microlattices have alumina thicknesses from ~40 to 210 nm, with an example shown in Fig. 2, D and H, with corresponding material weight density ranging from less than 1 kg/m³ to 10.2 kg/m³.

Loading the resin bath with nanoparticles can further expand the base material set. Solid Al_2O_3 ceramic lattices were prepared in the microlithography system by using photosensitive PEGDA liquid prepolymer loaded with ~150-nm alumina nanoparticles (Baikowski Inc., ~12.5% alumina by volume). The same sequential lithographic exposure process produced a microlattice made of a hybrid of solid PEGDA and alumina

nanoparticles. These hybrid lattices are converted to pure Al_2O_3 octet-truss microlattices through a sintering procedure (39). An example of this structure is shown in Fig. 2, E and I. The parameters and properties for a selection of our stretch-dominated mechanical metamaterials and bend-dominated foams are summarized in table S1. The densities of all samples were calculated by measuring the weight and fabricated dimensions of the completed microlattices.

The microstructured mechanical metamaterials were tested to determine their Young's modulus E and uniaxial compressive strength σ_y, defined as the crushing stress of the material. Uniaxial compression studies of all microlattices with the same cubic dimensions were conducted on an MTS Nano Indenter XP, equipped with a flat punch stainless steel tip with a diameter of 1.52 mm. During 20 consecutive compression cycles up to 10% strain, we observed typical viscoelastic behavior for the polymer microlattices with pronounced hysteresis and loading rate–dependent Young's modulus. The Young's moduli for all polymer microlattices and foams were extracted at a loading rate at 87.2 nN/s,

corresponding to a strain rate of 10^{-3} s^{-1}. Uniaxial compression of these structures is shown in movies S1 to S3. Representative stress-strain curves from uniaxial compression crushing tests for determining the compressive strength of octet-truss microlattices made of solid HDDA polymer, hollow-tube Ni-P metal, and solid alumina are shown in fig. S7, A and B, and fig. S8A, respectively. Bulk HDDA polymer, cured by UV cross-linking a solid sample of similar dimensions to the octet-truss lattices, was determined to have Young's modulus $E_s = 530$ MPa and yield stress $\sigma_{ys} = 86$ MPa. [See (39) for detailed measurement methods and bulk property values for other constituent materials.]

The results of these mechanical tests, together with the bend-dominated tetrakaidecahedron-based Kelvin foams fabricated from the base HDDA polymer, are summarized in Fig. 3, A and B, which respectively plot relative Young's modulus and strength against relative mass density. Figure 4 shows the location of these material properties on the stiffness versus density material selection chart, together with other recently reported ultralight materials for comparison. The stretch-dominated microlattices populate the highly desirable ultralight, ultrastiff space toward the upper left of the chart (17) and have stiffness-to-weight ratios that do not substantially degrade as density decreases by several orders of magnitude. In contrast to the common bend-dominated $E/E_s \propto (\rho/\rho_s)^2$ scaling of open-cell stochastic foams such as silica aerogels and carbon foams, our stretch-dominated microlattice materials demonstrate the desired linear relationship of $E/E_s \propto \rho/\rho_s$, approaching the theoretical limit, and exhibit this remarkable scaling relationship over three orders of magnitude in density and across all constituent materials studied. These octet-truss lattice materials are highly isotropic, so the scaling of stiffness with density does not vary with the orientation of the lattice (fig. S4), as confirmed by our studies of different loading directions. These lattices have the highest specific stiffness when the lattice is loaded normal to the (111) plane, which is closest-packed within the fcc architecture.

In the ultralow-density regime (relative density <0.1%), we observed markedly different compression behavior in hollow-tube ALD ceramic octet-truss microlattices relative to solid ceramic lattices at higher relative densities (8 to 20%). The hollow-tube ceramic microlattices with nanoscale wall thicknesses showed smoother behavior with progressively fewer discontinuities in their stress-strain curves (fig. S8, A and B), in contrast to solid microstrut ceramic lattices with catastrophic, fracture-dominated behavior. The loading-unloading curves of hollow-tube Al_2O_3 lattices revealed elastic behavior followed by a nonlinear response on each loading cycle. Although relative compressive stiffness and relative density initially follow a nearly linear scaling law, the transition from conventional brittle behavior (in low-density ceramic materials) to more "ductile" mechanical behavior (in ultralight materials with nanoscale wall thicknesses) suggests
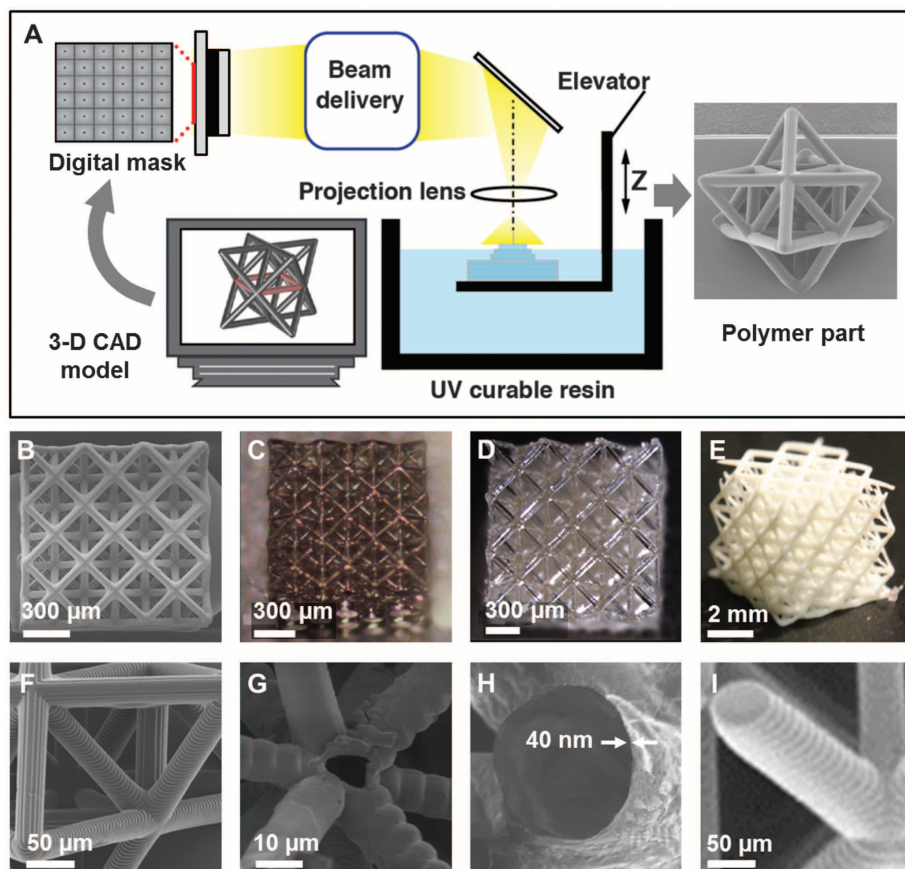

Fig. 2. Fabrication of ultralight, ultrahigh-stiffness stretch-dominated microlattices. (**A**) Projection microstereolithography, a layer-by-layer technique capable of fabricating arbitrary, microscale, three-dimensional structures with resolution of ~5 μm. As the structure builds, the substrate is lowered into the liquid resin by an elevator traveling vertically (marked as Z-direction); the SEM image at the right is the fabricated octet-truss unit cell. (**B** to **E**) Octet-truss microlattices with varied constituent materials and configurations: (B) solid polymer HDDA; (C) hollow-tube metallic Ni-P; (D) hollow-tube ceramic (alumina); (E) solid ceramic (alumina). (**F** to **I**) Magnified views of the struts of the microlattices in (B) to (E), respectively.

Fig. 3. Measurement of the material properties of stretch-dominated microlattices and Kelvin foams as a function of relative density. (**A**) Relative stiffness as a function of relative density for stretch-dominated and bend-dominated microlattices. Stretch-dominated materials exhibit a linear stiffness-density relationship of $E \propto \rho$, whereas bend-dominated materials soften as $E \propto \rho^2$ or worse, as shown by their slopes in the plot. (**B**) Relative strength as a function of relative density for stretch-dominated and bend-dominated microlattices.

a transition from a fracture-dominated failure mode to a buckling-dominated failure mode, with suppression of the catastrophic failure seen in solid Al_2O_3 octet-truss lattices.

These differences in compressive behavior between solid and hollow-tube ceramic octet-truss lattices are primarily attributed to local buckling induced by the high aspect ratio of the strut length to nanoscale wall thickness, in contrast to nanoscale TiN trusses (*32*) and ceramic composite (*34*), whose aspect ratios are low enough to allow the nanoscale strengthening effect of the wall thickness to dominate. For example, the ratio of strut length to nanoscale wall thickness in fig. S8B is about 1400:1 and contributes to its large compression strain, governed by $\varepsilon \propto (1/\rho)^{0.5}$ (*17*). Thus, the relative compressive strength makes a transition from the nearly linear scaling law governing the stretch-dominated failure mode at an approximate density near 0.08% to a scaling power of 2.7, as indicated in Fig. 3B. In the same figure, a similar transition from yielding-dominated to buckling-dominated failure at an approximate relative density of 0.2% is evident in Ni-P lattices, consistent with the trend observed for bend-dominated metallic microlattices (*26*).

When an ultralow-density metallic microlattice is bend-dominated, its stiffness degrades substantially with reduced density. An example of this is the Ni-P lattice reported by Schaedler *et al.* (*20*), whose specific stiffness (stiffness-to-weight ratio) degrades from 0.23×10^6 m^2/s^2 to 0.05×10^6 m^2/s^2 as density is reduced from 40 mg/cm^3 to 14 mg/cm^3 (*45*). By contrast, our Ni-P stretch-dominated metallic lattice is not only much stiffer in the same density range, its specific stiffness stays nearly constant, measured as 1.8×10^6 m^2/s^2 and 2.1×10^6 m^2/s^2 at densities of 14 mg/cm^3 and 40 mg/cm^3, respectively. Similarly, in a recent report of high-strength microarchitected ceramic composites (*34*), their strength performance approaches the linear scaling relationship over a narrow density range, and only when loaded in a direction optimized for their anisotropic architecture. Our metamaterials, in contrast, maintain their mechanical efficiency over a broad density regime without substantial degradation in specific stiffness, owing to the nearly linear E-ρ scaling relationship.

We have shown that these high mechanical efficiencies are possible across a range of constituent materials. Fabricating ordered lattice structures at these length scales brings them into the regime in which it becomes possible to design microstructured functional materials with superior bulk-scale properties.
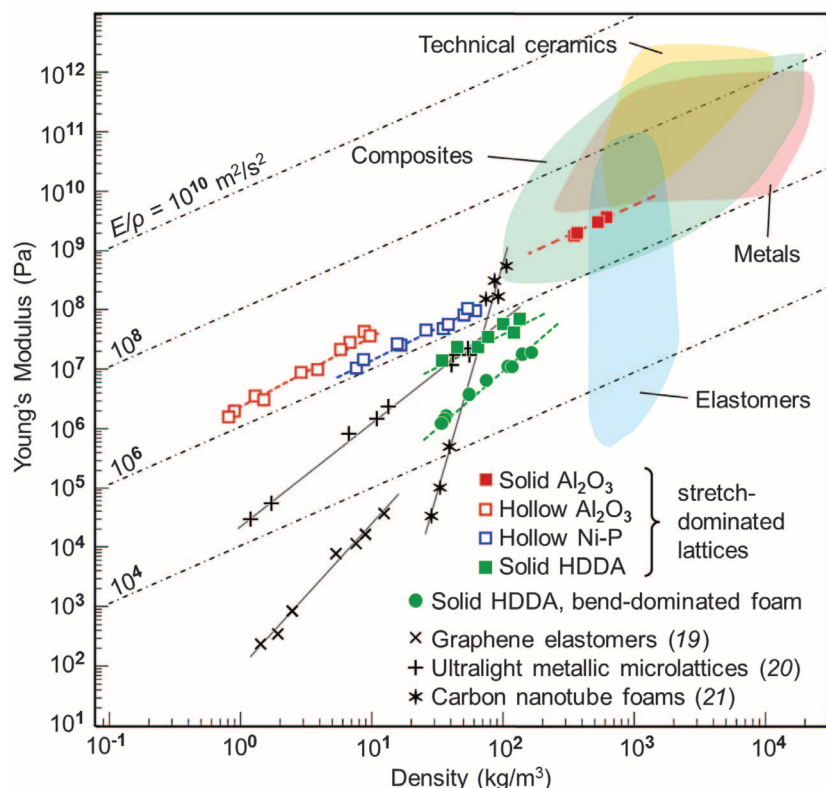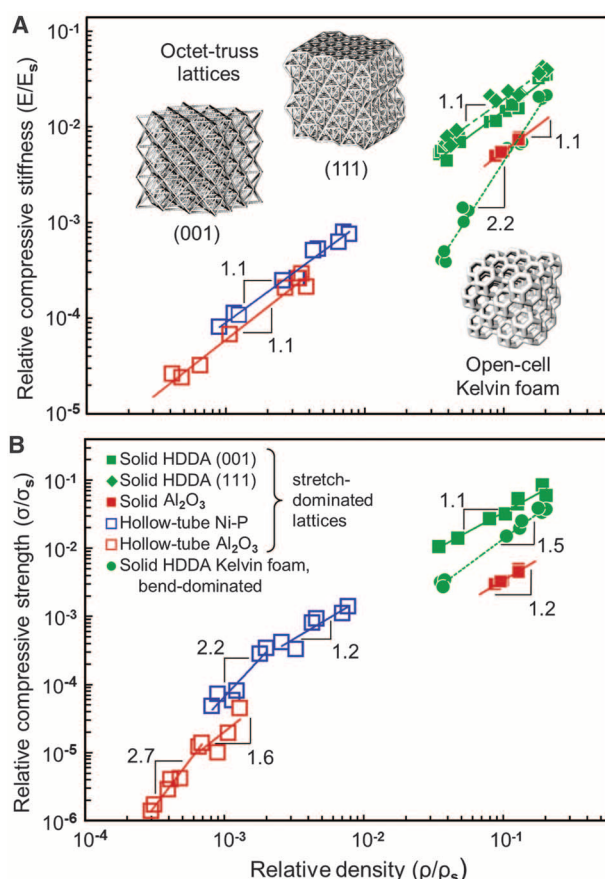

Fig. 4. An Ashby chart plotting compressive stiffness versus density for ultralight, ultrastiff mechanical metamaterials and other previously reported materials. Dotted lines indicate contours of constant stiffness-density ratio $c = E/\rho$ (m^2/s^2).

REFERENCES AND NOTES

1. K. Ando, H. Onda, *J. Wood Sci.* **45**, 120–126 (1999).
2. T. M. Ryan, C. N. Shaw, *Proc. R. Soc. B* **280**, 20130172 (2013).
3. P. Van Liedekerke *et al.*, *Phys. Biol.* **7**, 026006 (2010).
4. J. H. Shen, Y. M. Xie, X. D. Huang, S. W. Zhou, D. Ruan, *Key Eng. Mater.* **535–536**, 465–468 (2013).
5. J. A. Kepler, *Compos. Sci. Technol.* **71**, 46–51 (2011).
6. L. Valdevit, A. J. Jacobsen, J. R. Greer, W. B. Carter, *J. Am. Ceram. Soc.* **94**, s15–s34 (2011).
7. N. Lyu, B. Lee, K. Saitou, *J. Mech. Des.* **128**, 527 (2006).
8. T. A. Schaedler *et al.*, *Adv. Eng. Mater.* **16**, 276–283 (2014).

9. K. J. Maloney et al., APL Mater. **1**, 022106 (2013).
10. L. Valdevit, A. Pantano, H. A. Stone, A. G. Evans, Int. J. Heat Mass Transfer **49**, 3819–3830 (2006).
11. M. Q. Li, X. Shi, Rare Metal Mater. Eng. **36**, 575 (2007).
12. O. Y. Kwon, H. J. Ryu, S. Y. Jeong, J. Ind. Eng. Chem. **12**, 306 (2006).
13. R. A. Olson, L. C. B. Martins, Adv. Eng. Mater. **7**, 187–192 (2005).
14. P. Day, H. Kind, Mod. Cast. **74**, 16 (1984).
15. S. Baudis et al., Biomed. Mater. **6**, 055003 (2011).
16. K. Arcaute, B. K. Mann, R. B. Wicker, Tissue Eng. C **17**, 27–38 (2010).
17. J. L. Gibson, F. M. Ashby, Cellular Solids: Structure and Properties (Cambridge Univ. Press, Cambridge, 2001).
18. H. Fan et al., Nat. Mater. **6**, 418–423 (2007).
19. L. Qiu, J. Z. Liu, S. L. Y. Chang, Y. Wu, D. Li, Nat. Commun. **3**, 1241 (2012).
20. T. A. Schaedler et al., Science **334**, 962–965 (2011).
21. M. A. Worsley, S. O. Kucheyev, J. H. Satcher, A. V. Hamza, T. F. Baumann, Appl. Phys. Lett. **94**, 073115 (2009).
22. T. M. Tillotson, L. W. Hrubesh, J. Non-Cryst. Solids **145**, 44–50 (1992).
23. S. O. Kucheyev et al., Adv. Mater. **24**, 776–780 (2012).
24. L. J. Gibson, MRS Bull. **28**, 270–274 (2003).
25. K. Tantikom, Y. Suwa, T. Aizawa, Mater. Trans. **45**, 509–515 (2004).
26. A. Torrents, T. A. Schaedler, A. J. Jacobsen, W. B. Carter, L. Valdevit, Acta Mater. **60**, 3511–3523 (2012).
27. C. Q. Dam, R. Brezny, D. J. Green, J. Mater. Res. **5**, 163–171 (1990).
28. J. K. Cochran, K. J. Lee, D. McDowell, T. Sanders, Multifunctional metallic honeycombs by thermal chemical processing. In Processsing and Properties of Lightweight Cellular Metals and Structures, A. K. Ghosh, T. H. Sanders, T. D. Claar, Eds. (Minerals, Metals and Materials Society, Seattle, WA, 2002), p. 127–136.
29. J. Zhang, M. F. Ashby, Int. J. Mech. Sci. **34**, 475–489 (1992).
30. D. Rayneau-Kirkhope, Y. Mao, R. Farr, Phys. Rev. Lett. **109**, 204301 (2012).
31. K. C. Cheung, N. Gershenfeld, Science **341**, 1219–1221 (2013).
32. D. Jang, L. R. Meza, F. Greer, J. R. Greer, Nat. Mater. **12**, 893–898 (2013).
33. L. Meza, J. Greer, J. Mater. Sci. **49**, 2496–2508 (2014).
34. J. Bauer, S. Hengsbach, I. Tesari, R. Schwaiger, O. Kraft, Proc. Natl. Acad. Sci. U.S.A. **111**, 2453–2458 (2014).
35. V. S. Deshpande, N. A. Fleck, M. F. Ashby, J. Mech. Phys. Solids **49**, 1747–1769 (2001).
36. J. D. Renton, Elastic Beams and Frames (Horwood, Chichester, UK, ed. 2, 2002).
37. S. Hyun, J. E. Choi, K. J. Kang, Comput. Mater. Sci. **46**, 73–82 (2009).
38. H. L. Fan, F. N. Jin, D. N. Fang, Mater. Des. **30**, 511–517 (2009).
39. See supplementary materials on Science Online.
40. W. Y. Jang, S. Kyriakides, A. M. Kraynik, Int. J. Solids Struct. **47**, 2872–2883 (2010).
41. Y. Takahashi, D. Okumura, N. Ohno, Int. J. Mech. Sci. **52**, 377–385 (2010).
42. X. Zheng et al., Rev. Sci. Instrum. **83**, 125001 (2012).
43. C. Sun, N. Fang, D. M. Wu, X. Zhang, Sens. Actuators A **121**, 113–120 (2005).
44. A. J. Jacobsen, W. Barvosa-Carter, S. Nutt, Adv. Mater. **19**, 3892–3896 (2007).
45. L. M. Moreau et al., Nano Lett. **12**, 4530–4539 (2012).

NANOMATERIALS

Long-range orientation and atomic attachment of nanocrystals in 2D honeycomb superlattices

M. P. Boneschanscher,[1] W. H. Evers,[2,3] J. J. Geuchies,[1] T. Altantzis,[4]
B. Goris,[4] F. T. Rabouw,[1] S. A. P. van Rossum,[1] H. S. J. van der Zant,[3]
L. D. A. Siebbeles,[2] G. Van Tendeloo,[4] I. Swart,[1] J. Hilhorst,[5] A. V. Petukhov,[1]
S. Bals,[4] D. Vanmaekelbergh[1]*

Oriented attachment of synthetic semiconductor nanocrystals is emerging as a route for obtaining new semiconductors that can have Dirac-type electronic bands such as graphene, but also strong spin-orbit coupling. The two-dimensional (2D) assembly geometry will require both atomic coherence and long-range periodicity of the superlattices. We show how the interfacial self-assembly and oriented attachment of nanocrystals results in 2D metal chalcogenide semiconductors with a honeycomb superlattice. We present an extensive atomic and nanoscale characterization of these systems using direct imaging and wave scattering methods. The honeycomb superlattices are atomically coherent and have an octahedral symmetry that is buckled; the nanocrystals occupy two parallel planes. Considerable necking and large-scale atomic motion occurred during the attachment process.

In oriented attachment, a single nanocrystal (NC) is formed from two adjacent NCs through atomically matched bond formation between two specific facets. Controlled oriented attachment is currently emerging as a route to form extended one- and two-dimensional single-crystalline semiconductors of II-VI and IV-VI compounds (1–5). These superlattices are of interest in optoelectronics. Truncated nanocubes of the Pb-chalcogenide family (fig. S1) have been recently used to create two-dimensional (2D) atomically coherent ultrathin quantum wells (4) as well as superlattices with square or honeycomb geometries (fig. S2) (5). The formation of such systems is remarkable, given that several demanding conditions must be fulfilled. The NC building blocks must be nearly monodisperse in size and shape, and attachment should only occur with a geometrically defined subset of NC facets. The long-range atomic and nanoscale order in such systems is far from understood. For extended, atomically coherent PbSe superlattices with honeycomb geometry, immediate questions emerge regarding the large-scale crystallographic orientation of the NCs, the role of surface passivation of specific facets, and the atomic mechanism of attachment.

Here, we report on the atomic and nanoscale analysis of atomically coherent PbSe, PbS, and CdSe honeycomb superlattices. Using high-angle annular dark-field scanning transmission electron microscopy (HAADF-STEM) tomography, we show that the honeycomb structures are buckled—the NCs occupy two parallel planes—and hence show nanoscale analogy with the proposed atomic silicene honeycomb structure. The specific orientation of the NCs in the 2D superlattice extends over hundreds of unit cells, suggesting that such types of single crystals must be formed from a preordered state, for example at the suspension/air interface. Compared with the native building blocks, the NCs in the honeycomb structure are considerably elongated in the direction of the NC-NC bond. This finding points to bond formation via necking accompanied with a gradual release of the capping molecules and considerable atomic motion within the NCs. Moreover, the 2D honeycomb structures of PbSe with a rocksalt atomic lattice were robust enough to be transformed into 2D CdSe lattices with a zinc blende atomic lattice through cation-exchange and keep the nanoscale honeycomb geometry intact. This method opens a route to a new class of 2D semiconductors with tunable composition. In these structures, the nanoscale honeycomb geometry has been predicted to result in both valence and conduction bands that can be filled with Dirac-type charge carriers as in graphene but, unlike graphene, with strong spin-orbit coupling (6).

The PbSe NCs have the shape of a cantellated cube, approaching that of a rhombicuboctahedron (fig. S1), implying that the NCs are terminated with {100}, {110}, and {111} facets. We estimated the NC size from the radially averaged diameter of the TEM projections for >1000 particles (5.3 ± 0.4 nm) (fig. S3). The oriented attachment of these NCs resulted in structures with long-range periodicity, as visualized by means of an equilateral triangle spanning the same number of unit cells along each vertex in the HAADF-STEM image (Fig. 1A).

[1]Debye Institute for Nanomaterials Science, University of Utrecht, Post Office Box 80.000, 3508 TA Utrecht, Netherlands. [2]Opto-electronic Materials Section, Delft University of Technology, Julianalaan 136, 2628 BL Delft, Netherlands. [3]Kavli Institute of Nanoscience, Delft University of Technology, Post Office Box 5046, 2600 GA Delft, Netherlands. [4]Electron Microscopy for Materials Science (EMAT), University of Antwerp, Groenenborgerlaan 171, 2020 Antwerp, Belgium. [5]European Synchrotron Radiation Facility (ESRF), Grenoble, Beamline ID01, France.
*Corresponding author. E-mail: d.vanmaekelbergh@uu.nl

Ultralight, ultrastiff mechanical metamaterials

Xiaoyu Zheng, Howon Lee, Todd H. Weisgraber, Maxim Shusteff, Joshua DeOtte, Eric B. Duoss, Joshua D. Kuntz, Monika M. Biener, Qi Ge, Julie A. Jackson, Sergei O. Kucheyev, Nicholas X. Fang, and Christopher M. Spadaccini

Microlattices make marvelous materials

Framework or lattice structures can be remarkably strong despite their very low density. Using a very precise technique known as projection microstereolithography, Zheng *et al.* fabricated octet microlattices from polymers, metals, and ceramics. The design of the lattices meant that the individual struts making up the materials did not bend under pressure. The materials were therefore exceptionally stiff, strong, and lightweight.

Science, this issue p. 1373

View the article online
https://www.science.org/doi/10.1126/science.1252291
Permissions
https://www.science.org/help/reprints-and-permissions

Use of this article is subject to the Terms of service